Comparative Tensor Visualisation within the Framework of Consistent Time-Stepping Schemes

R. Mohr[1], T. Bobach[2], Y. Hijazi[2], G. Reis[2], P. Steinmann[1], and H. Hagen[2]

[1] University of Kaiserslautern
Chair of Applied Mechanics
Department of Mechanical and Process Engineering
D-67653 Kaiserslautern, Germany
http://mechanik.mv.uni-kl.de

[2] University of Kaiserslautern
Computer Graphics Group
Department of Computer Sciences
D-67653 Kaiserslautern, Germany
http://www-hagen.informatik.uni-kl.de

Abstract: Nowadays, the design of so-called consistent time-stepping schemes that basically feature a physically correct time integration, is still a state-of-the-art topic in the area of numerical mechanics. Within the proposed framework for finite elasto-plasto-dynamics, the spatial as well as the time discretisation rely both on a Finite Element approach and the resulting algorithmic conservation properties have been shown to be closely related to quadrature formulas that are required for the calculation of time-integrals. Thereby, consistent integration schemes, which allow a superior numerical performance, have been developed based on the introduction of an enhanced algorithmic stress tensor, compare [MMS06]-[MMS07c].
In this contribution, the influence of this consistent stress enhancement, representing a modified time quadrature rule, is analysed for the first time based on the spatial distribution of the tensor-valued difference between the standard quadrature rule, relying on a specific evaluation of the well-known continuum stresses, and the favoured non-standard quadrature rule, involving the mentioned enhanced algorithmic stresses. This comparative analysis is carried out using several visualisation tools tailored to set apart spatial and temporal patterns that allow to deduce the influence of both step size and material constants on the stress enhancement. The resulting visualisations indeed confirm the physical intuition by pointing out locations where interesting changes happen in the data.

1 Motivation

It is well-known in literature that the performance of classical time integration schemes for structural dynamics, as for instance developed in [New59], is strongly limited when dealing with highly nonlinear systems. In a nonlinear setting, sophisticated numerical techniques are required to satisfy the classical balance laws, as for instance balance of

linear and angular momentum or the classical laws of thermodynamics. Nowadays, energy and momentum conserving time integrators for dynamical systems, like multibody systems or elasto-dynamics, are well-established in the computational dynamics community, compare e.g. [ST92]. In contrast to the commonly used time discretisation based on Finite Differences, one-step implicit integration algorithms relying on Finite Elements in space and time were developed, for instance, in Betsch and Steinmann [BS01]. Therein, conservation of energy and angular momentum have been shown to be closely related to quadrature formulas required for numerical integration in time. In this context, specific algorithmic energy conserving schemes for hyperelastic materials can be based on the introduction of an enhanced stress tensor for time shape functions of arbitrary order, compare Gross *et al.* [GBS05]. Recently, a generalisation of these Galerkin-based concepts to finite elasto-plasto-dynamics has been worked out by Mohr *et al.* [MMS06]-[MMS07c].

However, it has been shown by many authors that the introduction of a modified stress tensor represents an appropriate tool to design specific conserving respectively consistent time-stepping schemes, compare e.g. [Arm06, Gonz00, GBS05, ML02a, MMS07c, NSP06]. Nevertheless, in our opinion the influence of this stress enhancement is not completely understood yet. One very interesting aspect that has not been addressed in the literature so far, is for instance the spatial distribution of the difference tensor between the stresses of the continuum model and the enhanced stresses for the time-stepping. In this context, we have already encouraged some basic discussions in [MMS06] based on an 'ad hoc' visualisation approach that provides very limited information. In this contribution, several more sophisticated techniques that offer different levels of detail regarding the included information, have been developed to visualise the difference between both second-order tensor fields. It will be demonstrated by means of representative parameter studies that the proposed concepts indeed represent an effective tool to better understand the numerical behaviour of the underlying time-stepping scheme.

2 Finite Elasto-Plasto-Dynamics

First, the nonlinear deformation map $\boldsymbol{\varphi}(\boldsymbol{X},t) : \mathcal{B}_0 \times [0,T] \rightarrow \mathcal{B}_t$ is introduced as a mapping from the material to the spatial configuration, whereby $\mathcal{B}_{0/t} \subset \mathbb{R}^{2/3}$. In the context of finite plasticity, the resulting deformation gradient $\boldsymbol{F} := \nabla_{\boldsymbol{X}} \boldsymbol{\varphi}(\boldsymbol{X},t)$ is assumed to be multiplicatively decomposed into an elastic and a plastic part:

$$\boldsymbol{F} \doteq \boldsymbol{F}_e \cdot \boldsymbol{F}_p \tag{1}$$

In contrast to the modelling of elasticity, additional internal variables $\boldsymbol{\kappa}$ are included in the Helmholtz energy density $\psi(\boldsymbol{F},\boldsymbol{\kappa})$ for the plastic case to model the loading history. Moreover, it is accepted to introduce the so-called conjugated thermodynamical forces $\boldsymbol{\beta} := -\nabla_{\boldsymbol{\kappa}}\psi$ which render the dissipation inequality, namely $\mathcal{D} = \left\langle \boldsymbol{\beta}, \dot{\boldsymbol{\kappa}} \right\rangle \geq 0$. In view of a thermodynamically consistent modelling this dissipation inequality has to be respected not only by the continuum model, but also by the applied numerical integration scheme. In a next step, we apply a standard Finite Element discretisation in space for the material

configuration of a solid continuum body. Using the spatial approximations, the semi-discrete deformation map can be written by means of the spatial shape functions $N_A(\boldsymbol{X})$ in the form: $\boldsymbol{\varphi}(\boldsymbol{X},t) = \sum_{A=1}^{n_{node}} \boldsymbol{q}_A(t)\, N_A(\boldsymbol{X})$. Consequently, the approximations in space of the spatial velocity $\boldsymbol{v} := \sum_{A=1}^{n_{node}} \dot{\boldsymbol{q}}_A\, N_A$ and the right Cauchy-Green tensor

$$\boldsymbol{C} := \boldsymbol{F}^{\mathrm{t}} \cdot \boldsymbol{F} = \sum_{A,B=1}^{n_{node}} \boldsymbol{q}_A \cdot \boldsymbol{q}_B\, \nabla N_A \otimes \nabla N_B \tag{2}$$

can be computed straightforwardly. To obtain a semi-discrete system of equations of motion, we combine the placements of the spatial nodes $\boldsymbol{q} = [\boldsymbol{q}_1, ..., \boldsymbol{q}_{n_{node}}]^{\mathrm{t}}$ and the nodal generalised momenta $\boldsymbol{p} := \mathbb{M} \cdot \dot{\boldsymbol{q}} = [\boldsymbol{p}_1, ..., \boldsymbol{p}_{n_{node}}]^{\mathrm{t}}$ with the mass matrix $\mathbb{M}$ to the vector $\boldsymbol{z} := [\boldsymbol{q}, \boldsymbol{p}]^{\mathrm{t}}$. Furthermore, the sum of the kinetic energy $T(\boldsymbol{p}) = \frac{1}{2}\, \boldsymbol{p} \cdot \mathbb{M}^{-1} \cdot \boldsymbol{p}$, the free energy $\Psi = \int_{\mathcal{B}_0} \psi \, \mathrm{d}V$ and possibly an external potential V^{ext} is defined as $H(\boldsymbol{q}, \boldsymbol{p}; \boldsymbol{\kappa}) := T + \Psi + V^{ext}$. Inspired by the purely elastic case, the resulting equations of motion can still be written in a compact format of Hamilton-type

$$\dot{\boldsymbol{z}}(t) = \mathbb{J} \cdot \nabla_{\boldsymbol{z}} H(\boldsymbol{z}; \boldsymbol{\kappa}) \qquad \text{with} \qquad \nabla_{\boldsymbol{z}} H = \begin{bmatrix} \boldsymbol{F}^{int} - \boldsymbol{F}^{ext} \\ \\ \mathbb{M}^{-1} \cdot \boldsymbol{p} \end{bmatrix}, \tag{3}$$

wherein we have incorporated the symplectic matrix $\mathbb{J}$ and the internal load vector $\boldsymbol{F}^{int}(\boldsymbol{S})$, involving the Piola Kirchhoff stresses $\boldsymbol{S} = 2\, \nabla_{\boldsymbol{C}}\, \psi$. Next, the time discretisation of the semi-discrete system of equations of motion (3) is considered. We start with a decomposition of the time interval $[0, T] = \bigcup_{n=0}^{N} [t_n, t_{n+1}]$ and a map of each sub-interval to the reference time interval $[0, 1]$ via the function $\alpha(t) := [t - t_n]/h_n$ based on the time-step size $h_n = t_{n+1} - t_n$. For the approximation in time a continuous Galerkin method – abbreviated by: cG(k)-method – is applied. Therefore, the time approximations of the unknown function $\boldsymbol{z}^h = \sum_{j=1}^{k+1} M_j(\alpha)\, \boldsymbol{z}_j$ and the test function $\delta \boldsymbol{z}^h = \sum_{i=1}^{k} \widetilde{M}_i(\alpha)\, \delta \boldsymbol{z}_i$ are introduced [1]. In a compact notation the resulting weak form in time is given by

$$\int_0^1 \left[\mathbb{J} \cdot \delta \boldsymbol{z}^h \right] \cdot \left[\mathrm{D}_\alpha \boldsymbol{z}^h - h_n\, \mathbb{J} \cdot \nabla_{\boldsymbol{z}} H(\boldsymbol{z}; \boldsymbol{\kappa}) \right] \mathrm{d}\alpha = 0\,. \tag{4}$$

Obviously, Equation (4) involves time-integrated internal load vectors, which will be referred to as $\bar{\boldsymbol{F}}^{int}_{A\,i}$ related to the spatial node A. As discussed for instance in Mohr *et al.* [MMS06]-[MMS07c], the crucial aspect for the conservation properties of the resulting time-stepping schemes is the approximation of these highly nonlinear time integrals. Of course, one potential option concerning the approximation is the application of a standard Gauss quadrature rule represented by

$$\bar{\boldsymbol{F}}^{int}_{A\,i} \approx \sum_{l=1}^{n_{gpt}} \sum_{B=1}^{node} w_l\, \widetilde{M}_i(\zeta_l)\, \boldsymbol{q}^h_B(\zeta_l) \left[\int_{\mathcal{B}_0} \nabla N_A \otimes \nabla N_B : \boldsymbol{S}\, \mathrm{d}V \right] \Big|_{\zeta_l}, \tag{5}$$

[1] It is important to emphasise that the time shape functions $M_j \in \mathcal{P}^k$ are polynomials of degree k, whereas the reduced shape functions $\widetilde{M}_i \in \mathcal{P}^{k-1}$ are only of degree $k-1$.

using the Gauss points ζ_l and the Gauss weights w_l. The foregoing discretisations render a completely discrete system of equations, representing a time-stepping scheme with the following conservation properties. If we assume vanishing external loads, the resulting integration scheme allows the conservation of linear momentum as well as the conservation of angular momentum. Nevertheless, it can be shown that such a standard quadrature rule is not able to guarantee the conservation of total energy for elastic deformations, despite being an essential feature which has to be captured by the integrator regarding the claimed thermodynamical consistency. Consequently, we introduce the nonstandard quadrature rule

$$\bar{\boldsymbol{F}}^{int}_{A\,i} \approx \sum_{l=1}^{n_{gp_t}} \sum_{B=1}^{node} w_l\, \widetilde{M}_i(\zeta_l)\, \boldsymbol{q}^h_B(\zeta_l) \left[\int_{\mathcal{B}_0} \nabla N_A \otimes \nabla N_B : \boldsymbol{S}^{alg}\, \mathrm{d}V \right] \Big|_{\zeta_l} , \tag{6}$$

wherein the so-called *elastic-enhanced algorithmic* stress tensor $\boldsymbol{S}^{alg} := \boldsymbol{S} + {}^{el}\boldsymbol{S}^{enh}$ has been applied based on the enhancement

$${}^{el}\boldsymbol{S}^{enh}(\boldsymbol{S}) = 2\, \frac{\psi_{\alpha=1} - \psi_{\alpha=0} - \int_0^1 \boldsymbol{S} : \frac{1}{2}\, \mathrm{D}_\alpha \boldsymbol{C}^h \ \mathrm{d}\alpha}{\int_0^1 || \,\mathrm{D}_\alpha \boldsymbol{C}^h ||^2 \ \mathrm{d}\alpha}\, \mathrm{D}_\alpha \boldsymbol{C}^h \ . \tag{7}$$

This approach follows the enhanced Galerkin methods – or short: eG(k)-methods – that have been proposed originally by Gross *et al.* [GBS05] in the context of hyperelasticity. Based on this specific nonstandard quadrature rule, the resulting time integrators guarantees additionally a conservation of the total energy $H_{\alpha=1} - H_{\alpha=0} = 0$ when the deformation is elastic. In combination with a strictly positive dissipation in the plastic case, a monotonic decrease of the total energy $H_{\alpha=1} - H_{\alpha=0} < 0$ and, consequently, a thermodynamically consistent time-integration can apparently be featured, offering superior performance in comparison to standard integration schemes. In this context, we want to point out once more that the key to thermodynamical consistency exclusively relies on a modified approximation of the corresponding time-integrals based on the elastic-enhanced algorithmic stress tensor.

3 Comparative Tensor Visualisation

In the previous section, the essential ingredients for a thermodynamically consistent time-integration have been presented. Thereby, the crucial difference between the standard Gauss quadrature rule and the more sophisticated nonstandard quadrature rule is directly related to the tensor-valued difference between the standard stresses of the continuum model $\boldsymbol{S}$ and the algorithmic stresses $\boldsymbol{S}^{alg}$, involving the enhancement tensor (7). One interesting aspect not addressed in literature so far is the spatial distribution of the corresponding difference tensor field. We are optimistic that such a comparison between both tensor fields provides a much deeper insight into the numerical behaviour of the related time-stepping schemes. In this context important issues are for instance: the correlation between the corrections and the underlying deformation, the influence of the time-step size

or the material properties, the evolution of the corrections in time, the existence of characteristic patterns within the difference tensor field, etc. However, a satisfying visualisation is a non-trivial task, dealing with two different tensor fields and a large number of time steps. A further difficulty is the fact that a direct physical interpretation of the enhancement term ${}^{el}\boldsymbol{S}^{enh}$ and the algorithmic stress tensor $\boldsymbol{S}^{alg}$, respectively, is not valid since it represents only a numerical tool to support the quadrature rule for time-integration. In the following, we focus on the development and the comparison of various visualisation approaches to better understand the influence of the correction on the time-quadrature rule.

To generate a benchmark data set, we calculated the motion of a 'Flying L' based on 36 4-node Finite Elements in space, using linear Finite Elements in time. For further set-up details we refer to Mohr *et al.* [MMS06]. In view of the abovementioned issues, the calculations have been performed with stiff/non-stiff material properties, involving $[\lambda, \mu] = [10000, 5000]/[1000, 500]$, and with large ($h_n = 0.4$) respectively small ($h_n = 0.04$) time-step sizes. Since the considered tensor fields are both defined in the reference configuration $\mathcal{B}_0$ only the undeformed configuration is of interest and, consequently, the actual deformation of the body is not shown, compare Figures 1- 10.

Figure 1 shows a visualisation obtained with Matlab by representing the tensor with its two orthogonal, normalised eigenvectors based on the spectral decompositions

$$\boldsymbol{S}^{alg} = \sum_{i=1}^{2} {}^{\boldsymbol{S}}\lambda_i^{alg}\, \boldsymbol{N}_i^{alg} \otimes \boldsymbol{N}_i^{alg} \qquad \text{and} \qquad \boldsymbol{S} = \sum_{i=1}^{2} {}^{\boldsymbol{S}}\lambda_i\, \boldsymbol{N}_i \otimes \boldsymbol{N}_i\,. \tag{8}$$

This figure was our initial motivation for experimenting with more advanced visualisations, especially to overcome the occlusion problem. Moreover, Figure 1 shows the two tensor fields and not its difference. However, a natural possibility to reduce the complexity of information is to find an appropriate representation of the difference field, since basically the corrections are of particular interest.

Our goal is to provide multiple different visualisation tools to support the understanding of both the spatial distribution of the algorithmic enhancement terms and their effect on the stress field. Therefore we examine the data in a spatial context from different points of view, one focusing on the magnitude of numerical differences in the stress tensors $\boldsymbol{S}$ and $\boldsymbol{S}^{alg}$ such as tensor invariants, another focusing on differences in extracted entities like principal stress directions. We combine basic visualisation techniques such as colour coding, transparency effects, and scaling together in order to provide the most helpful tools, thereby applying Information Visualisation [Jac99] techniques. Very little work has been carried out for difference tensor visualisation; most results relate to the tensor visualisation itself, which already is a challenge. Some examples include the visualisation of stress and strain tensors [GGH*97, NJP05] and the visualisation of diffusion tensor MRI [WMN*02].

We analyse a particular time step from abovementioned simulation for the combination of stiff/non-stiff material and fine/coarse time resolution, resulting in four different configurations. These are shown in Figure 2, showing the principal directions $[\boldsymbol{N}_i^{alg}, \boldsymbol{N}_i]$ in [blue, red] [2] similar to Figure 1. Since principal stress directions are not oriented, we use

[2] This is replaced by a [lighter,darker] grey in the b/w print.

line segments scaled by the magnitude of the corresponding eigenvalues to show the stress distribution over the elements. The scaling has been chosen to avoid the visual clutter seen in Figure 1, yet although both stresses are visualised, the absolute difference in these intuitive representations is too small to be seen, justifying the direct analysis of difference terms as proposed in the subsequent sections.

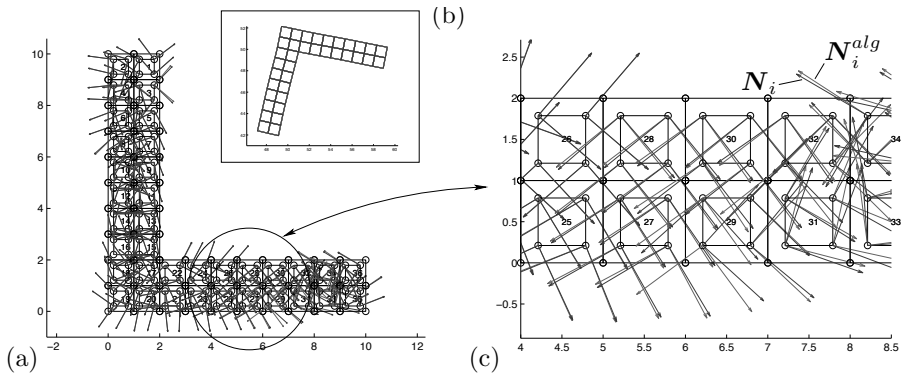

Figure 1: (a) reference configuration $\mathcal{B}_0$ with the eigenvectors $[\boldsymbol{N}_i^{alg}, \boldsymbol{N}_i]$ of the elastic-enhanced algorithmic stress tensor $\boldsymbol{S}^{alg}$ & the Piola Kirchhoff stress tensor $\boldsymbol{S}$, (b) deformed configuration $\mathcal{B}_t$ after $10s$, (c) zoom of the principal directions $[\boldsymbol{N}_i^{alg}, \boldsymbol{N}_i]$.

3.1 Interpreting the symmetric difference tensor field as a $3d$ vector field

We are interested in a way of representing the difference tensor field. Notice that the considered tensors are all symmetric so we have three independent components, i.e.

$$\boldsymbol{S} = \begin{bmatrix} S_{11} & S_{12} \\ S_{12} & S_{22} \end{bmatrix} \tag{9}$$

which we can represent as a $3d$ vector $s = [S_{11}\ S_{22}\ S_{12}]^{\mathrm{t}}$, similar to the classical Voigt notation in the Finite Element context.

We have chosen this approach since we find it much more intuitive to compute the difference between two vectors than computing the difference between two tensors. We then connected the $3d$ vectors of each Gauss point, four by four, to create patches resulting in a quad-patch for every calculation element. Even if the resulting patches are indeed $3d$ we find it useful to simply visualise their $2d$ projection, as it shows the deformations. Note that this type of deformation is not related to the physical deformation of the considered body. Based on this visualisation, we compensated the loss of one dimension by adding circles at each Gauss point whose radii are the Euclidean norm of the $3d$ difference vectors, namely $r = \sqrt{\Delta {S_{11}}^2 + \Delta {S_{22}}^2 + \Delta {S_{12}}^2}$. Figures 3(a,b) and 4(a,b) respectively illustrate

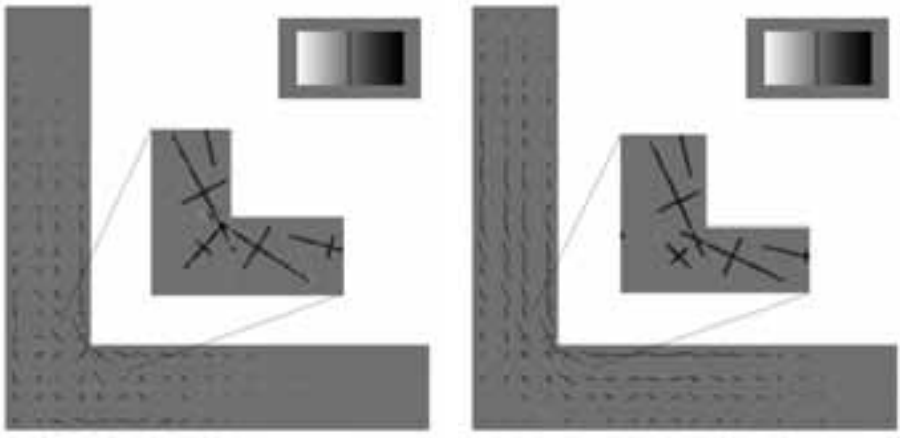

(a) stiff data set, $h_n = 0.4$, time step 11

(b) stiff data set, $h_n = 0.04$, time step 110

(c) non-stiff data set, $h_n = 0.4$, time step 11

(d) non-stiff data set, $h_n = 0.04$, time step 110

Figure 2: The stress configurations in question, where the lines depict the principal stress directions scaled by the magnitude of the corresponding eigenvalues.

those visualisations for stiff and non-stiff data sets[3].

The results clearly demonstrate that the proposed approach is considerably well-suited to highlight regions of the body in which large corrections occur, compare Figure 3(a). Moreover, it is obvious that the corrections are higher when large time-step sizes are involved, compare e.g. Figure 3(a) and Figure 3(b).

[3]Note that we used a linear scaling to avoid occlusion.

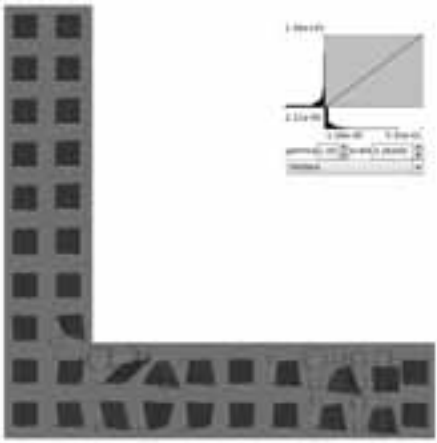

(a) stiff data set, $h_n = 0.4$, time step 11

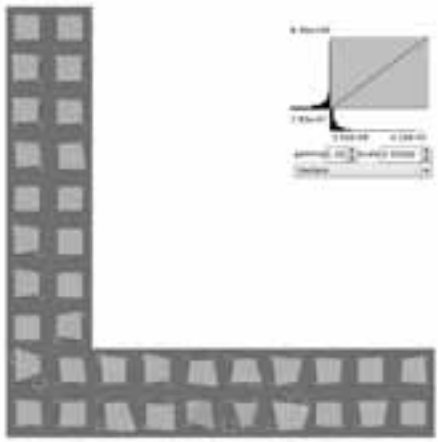

(b) stiff data set, $h_n = 0.04$, time step 110

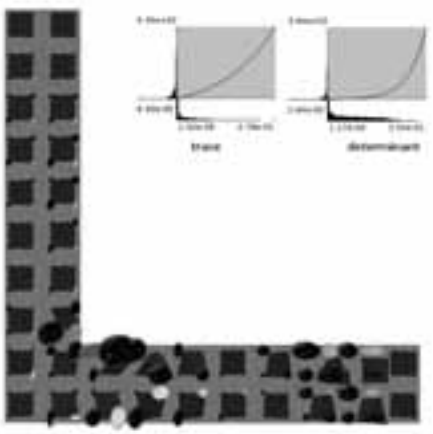

(c) stiff data set, $h_n = 0.4$, time step 11

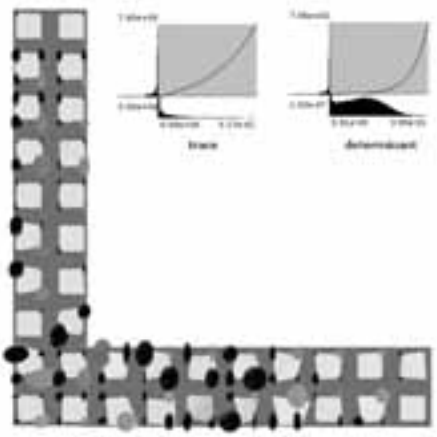

(d) stiff data set, $h_n = 0.04$, time step 110

Figure 3: Circle- and ellipsoid-based visualisation using *stiff* material properties.

3.2 Visualising the tensor invariants through ellipsoids

Another approach - more rigorous this time - consists of visualising the tensor invariants as ellipsoids. Despite looking very similar to Kindlmann's tensor glyphs [Kin04], our ellipsoids don't involve the tensor eigenvectors at all. The characteristic function of a tensor $\boldsymbol{S}$ is given by

$$\chi(\boldsymbol{S}) = |\boldsymbol{S} - \lambda \boldsymbol{I}| = \lambda^2 - [S_{11} + S_{22}]\lambda + [S_{11}S_{22} - {S_{12}}^2] \tag{10}$$

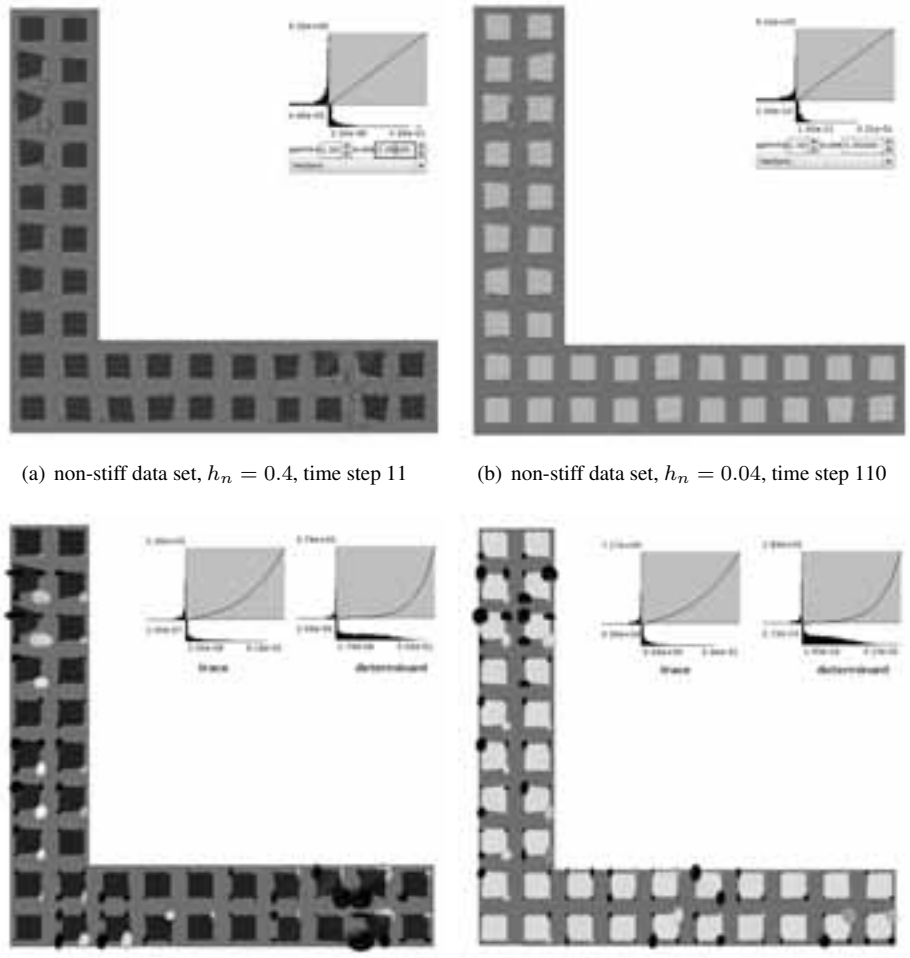

(a) non-stiff data set, $h_n = 0.4$, time step 11

(b) non-stiff data set, $h_n = 0.04$, time step 110

(c) non-stiff data set, $h_n = 0.4$, time step 11

(d) non-stiff data set, $h_n = 0.04$, time step 110

Figure 4: Circle- and ellipsoid-based visualisation using *non-stiff* material properties.

and provides two invariants, namely the trace and the determinant of the tensor:

$$I_1 = \text{tr}(\boldsymbol{S}) = S_{11} + S_{22} \quad \text{and} \quad I_2 = \det(\boldsymbol{S}) = S_{11}S_{22} - {S_{12}}^2. \tag{11}$$

The ellipsoid is built using the components' basis

$$(x, y, z) = (\Delta I_1, \Delta I_2, \frac{\Delta I_1 + \Delta I_2}{2}), \tag{12}$$

where ΔI_i is the difference between the invariants of both tensor fields.

Figures 3(c,d) and 4(c,d) respectively illustrate the ellipsoid-based visualisations for data sets that have been calculated by means of stiff and non-stiff material properties. Moreover, Figure 5 shows the evolution of the differences between the invariants over time. To investigate a potential correlation between the deformation and the corrections, the norm of the physical strain field based on the right Cauchy-Green strain tensor $\boldsymbol{C}$ has been additionally incorporated, where the following colour-coding has been used: from blue [lighter] to red [darker] for increasing strain norms. Note that we used a logarithmic scaling here, as opposed to a linear scaling, since the differences are much greater than in the circle-based visualisation[4]. In comparison to the previous approach, the corresponding plots provide an essentially better view on the spatial distribution of the corrections, since the regions with extremely large corrections are not so dominant due to the mentioned logarithmic scaling. In this context, it becomes obvious that the locations of the corrections are, especially for the stiff data set shown in Figure 3(c,d), more homogeneously distributed when a smaller time-step size is applied. Also very interesting is the clustering of large corrections in certain regions of the 'L' particularly where the norm of the strains is high, as pictured in Figure 5.

3.3 Interpreting the differences of physical measures

So far, focus has been on the display of abstract measures derived from numerical representations of the stress tensors that might be hard to interpret. We now turn our attention to changes in more physically motivated measures given by the eigenvectors $[\boldsymbol{N}_i^{alg}, \boldsymbol{N}_i]$, and eigenvalues $[{}^{\boldsymbol{S}}\lambda_i^{alg}, {}^{\boldsymbol{S}}\lambda_i]$ of both stress tensors $[\boldsymbol{S}^{alg}, \boldsymbol{S}]$, as already introduced in Equation (8). From a mechanical point of view, such a spectral decomposition is quite intuitive, since the results can be interpreted as principal stresses and principal stress directions respectively. Nevertheless, keep in mind that a direct physical interpretation of the algorithmic stress tensor by itself is critical. However, the actual goal is to show how the stress distribution is modified by the introduction of the correction term, related to Equation (7). We therefore consider rotation of the principal stress directions, and changes in the stress magnitude along these, whereby particularly the rotation seems to be an interesting issue in this context.

The computation of a rotation angle α_i between the principal directions requires the association of each direction in $\boldsymbol{N}_i^{alg}$ with a direction in $\boldsymbol{N}_i$. This can be based either on the minimisation of the variation in the corresponding eigenvalues or the minimisation of the angle between the directions. If these two criteria don't agree, say, both major eigenvalues are close but the major principal direction of the enhanced tensor aligns with the minor principal direction of the untouched tensor, the choice is arbitrary and leads to different magnitudes in angle or principal stress. In our considerations, we favour closely aligned principal directions over similar eigenvalues, where the largest eigenvalue of $\boldsymbol{S}$ determines the major principal direction. Finally, the difference in the absolute eigenvalues amounts to the root-mean-square error between the ordered pair of absolute eigenvalues in both the

[4]The redistribution caused by the logarithmic transfer function can be seen in the histograms displayed in the top-right corner.

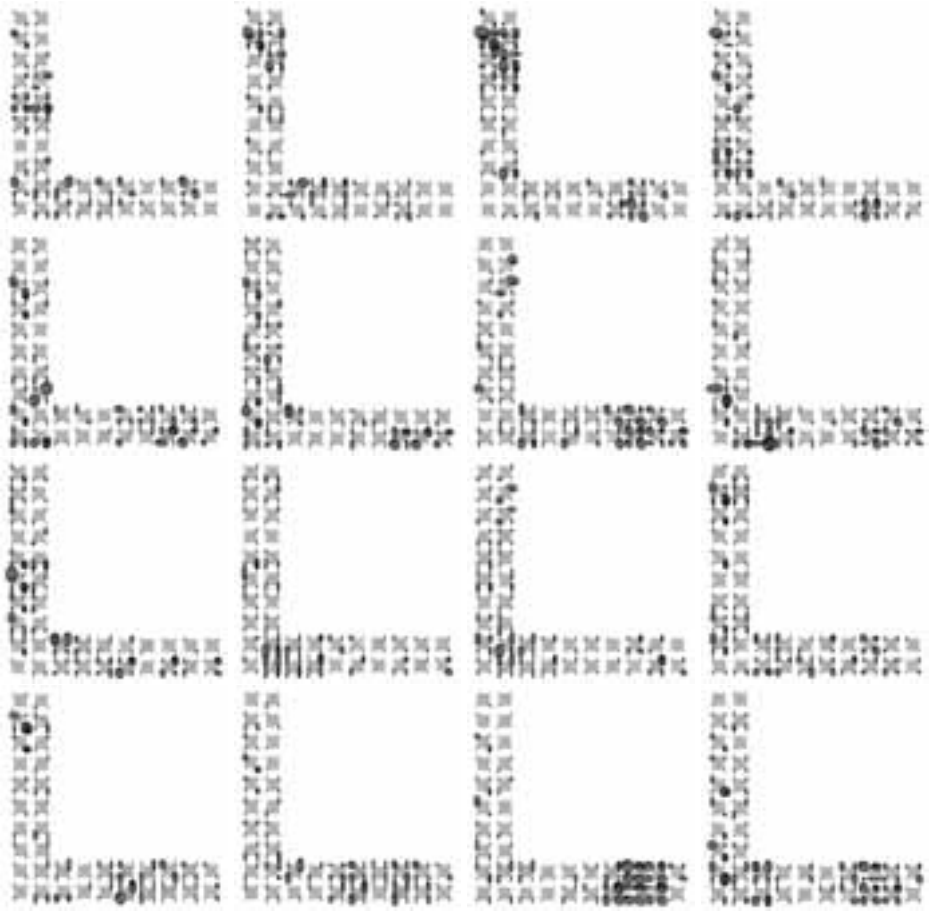

Figure 5: Ellipsoid-based visualisation over time. From top-left to bottom-right: time step 220 to 235.

enhanced and the basic stresses, rendering

$$\Delta\lambda := \left[(|^{\boldsymbol{S}}\lambda_1^{alg}| - |^{\boldsymbol{S}}\lambda_1|)^2 + (|^{\boldsymbol{S}}\lambda_2^{alg}| - |^{\boldsymbol{S}}\lambda_2|)^2 \right]^{\frac{1}{2}} . \tag{13}$$

3.3.1 Wedges as rotation indicators

As seen in Figure 2, the angular difference α_i between $[\boldsymbol{N}_i^{alg}, \boldsymbol{N}_i]$ is too small for direct visualisation purposes. We therefore propose an exaggerated display of those using wedges that indicate the rotation direction with a colour sweep as seen in Figures 6(a-d). Prior to display, the computed angles are equalised based on the transfer function

$$\tilde{\alpha}_i = \text{sign}(\alpha_i) \ \cdot \ \lambda|\alpha_i|^\gamma, \qquad \lambda, \gamma \in \mathbb{R}^+ . \tag{14}$$

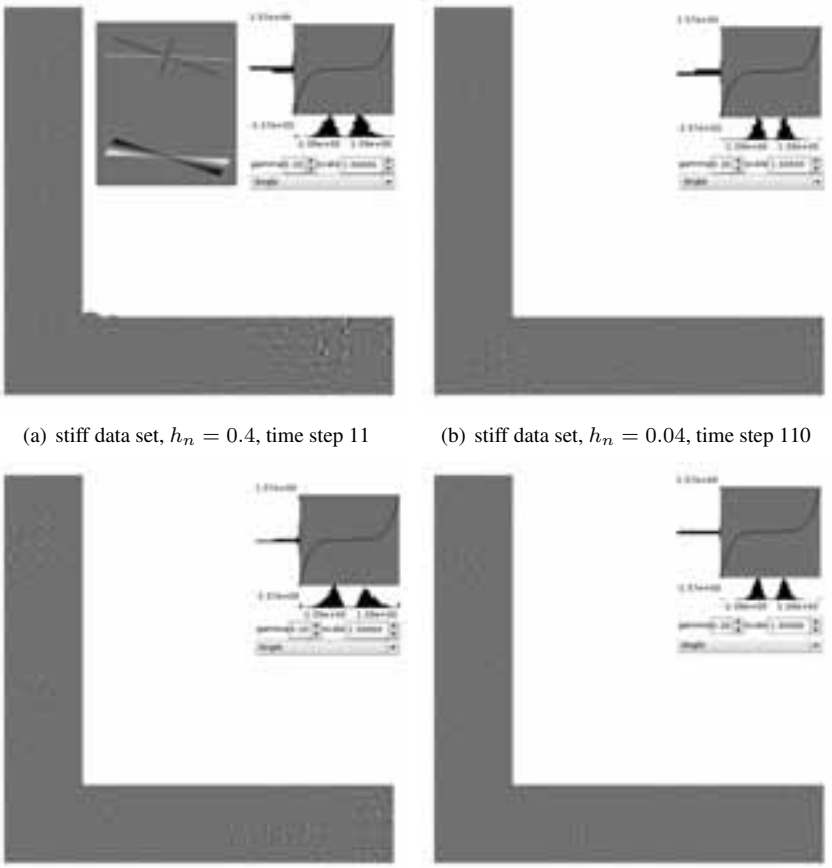

(a) stiff data set, $h_n = 0.4$, time step 11

(b) stiff data set, $h_n = 0.04$, time step 110

(c) non-stiff data set, $h_n = 0.4$, time step 11

(d) non-stiff data set, $h_n = 0.04$, time step 110

Figure 6: Wedge visualisation for *stiff* and *non-stiff* data at different time resolutions. The angles have been scaled such as to provide an exaggerated display of the qualitative behaviour.

Note that a choice of $\gamma = 1$ corresponds to linear scaling by λ, while for $\gamma < 1$, stretching occurs in the interval $[-1, 1]$ - which is a reasonable behaviour as $\alpha_i \in [-\pi/4, \pi/4]$. In the present example a choice of $\lambda = 1$ and $\gamma = 0.2$ led to the best results, the corresponding equalised angle distribution is shown in the top-right corner.

The visualisation in Figures 6(a-d) employs a uniform scaling of the major eigenvectors, because the screen space occupied by one such glyph directly correlates with the user-perceived importance. As the main objective is to indicate rotation, the change in the magnitude of eigenvalues has been mapped linearly to circles, which we found least distracting from the main visualisation goal.

Once more, the results confirm the fundamental influence of the applied time-step size: a

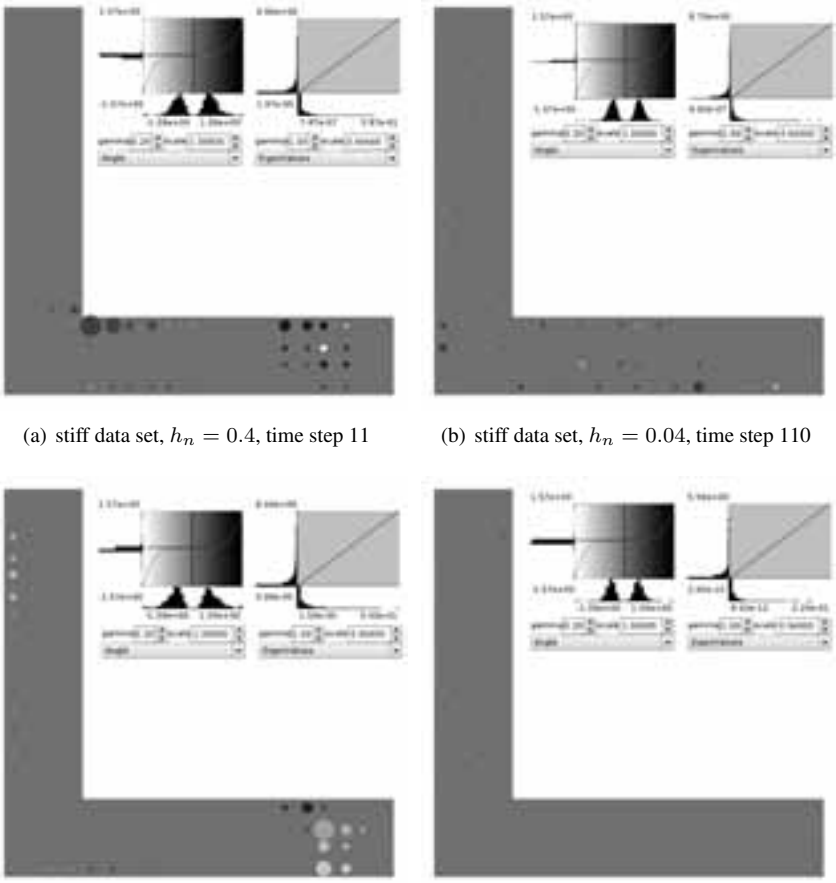

(a) stiff data set, $h_n = 0.4$, time step 11

(b) stiff data set, $h_n = 0.04$, time step 110

(c) non-stiff data set, $h_n = 0.4$, time step 11

(d) non-stiff data set, $h_n = 0.04$, time step 110

Figure 7: Colour-coded discs displaying the difference in the eigenvalues via diameter and angle modification via blue ($\alpha_i < 0$) and red ($\alpha_i > 0$) colour. In the b/w print, this is replaced by [lighter,darker] grey.

larger time-step size requires also larger corrections. Moreover, we can see that in some elements large modifications of the angle are combined with small changes in the eigenvalues and vice versa, compare Figure 6(a). Analogously to Figure 3(a,b) and Figure 4(a,b), it is obvious that for the present example the largest modifications are needed when stiff material properties are combined with large time-step sizes.

3.3.2 Colour-coded discs as indicators of change in eigenvalue magnitude

The wedge-based visualisation obviously lacked clarity with respect to the rotation direction due to the small size of the glyphs. A simple yet very effective visualisation of

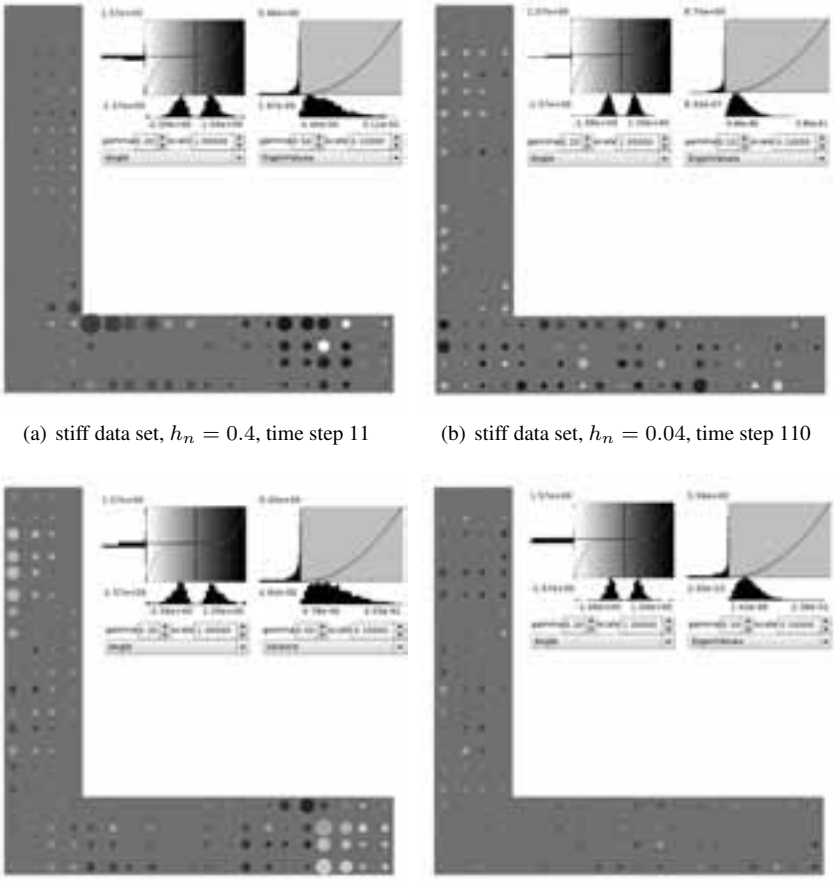

(a) stiff data set, $h_n = 0.4$, time step 11

(b) stiff data set, $h_n = 0.04$, time step 110

(c) non-stiff data set, $h_n = 0.4$, time step 11

(d) non-stiff data set, $h_n = 0.04$, time step 110

Figure 8: The same setting as in Figure 7, but now equalising the eigenvalues for all data sets based on the same transfer function. All but (b) exhibit better visible details.

sign and magnitude is achieved by colour-coding, where blue indicates negative rotation and red positive[5], see Figures 7 and 8. Here again an equalisation of the value range is necessary to address nuances in the angle distribution close to the origin.

We aim as a second aspect for the depiction of differences in the tensor eigenvalues, corresponding to the difference in the principal stress magnitude along $[\boldsymbol{N}_i^{alg}, \boldsymbol{N}_i]$. Figure 7 displays coloured discs with linearly scaled differences as radii. As can be seen in Figure 7(a,c), regions with dominant corrections can be immediately captured, especially for the large time-step size. However, the resulting visualisation only indicates changes in few tensors because of the large variation in magnitude of the displayed values, therefore

[5]This is replaced by a [lighter,darker] pattern in the b/w print.

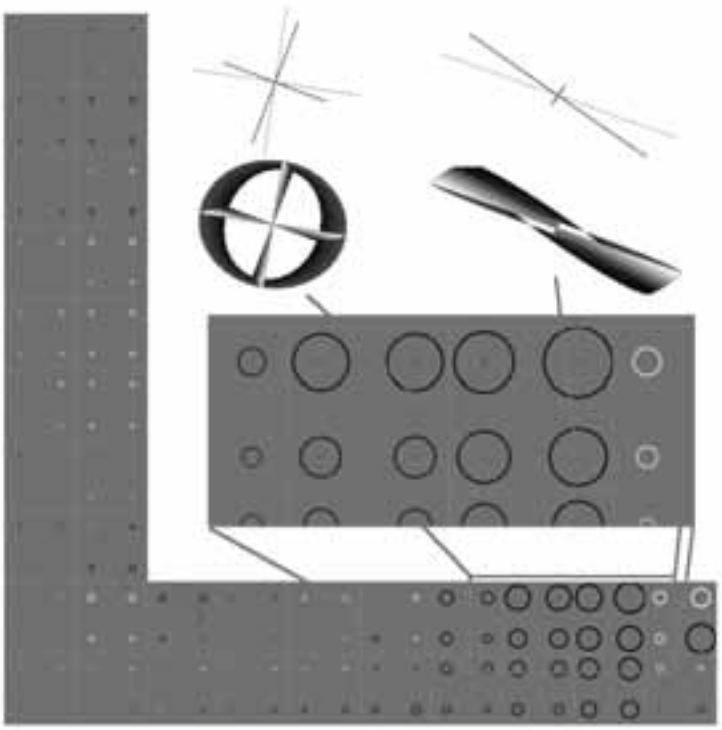

Figure 9: Level-of-detail visualisation, showing more qualitative facts at a large scale while depicting the concrete deformation on a per-tensor basis after an appropriate zoom. The pixel clutter visible in the angle of the 'L' is actually a swept ellipse similar to the one depicted in the second top row, yet very big and very thin (reproduced in colour on p. 189).

loosing more subtle details to the scaling.

This is taken care of by again equalising the value range as shown in Figure 8. The respective transfer functions are displayed in the top right corner of each figure. It can be seen in Figure 8(b) that the equalisation, if not properly scaled, obfuscates details as the result of a too uniform value distribution. Nevertheless, especially Figure 8 (a,c) enables a very interesting perspective on the spatial distribution of the modifications. Obviously, homogeneously coloured 'correction clusters' occur within the 'L', similar to the results of the ellipsoid-based visualisation.

3.3.3 Level-of-detail investigation using complex glyphs

The last approach we present is based on a multiresolution paradigm, providing qualitative information at a global scale while allowing to look at concrete behaviour in detail at an adequate zoom level. The large scale visualisation in Figure 9 combines the difference in

eigenvalues via the circle diameters, and the angle and direction of rotation via the circle colours. The detail level depicts the magnitude and angle modification as a sweep between individual representations of $\boldsymbol{S}^{alg}$ and $\boldsymbol{S}$.

The employed glyphs are created in the following way. Each pair $[\boldsymbol{N}_i^{alg}, \boldsymbol{N}_i]$ of principal directions, scaled by the eigenvalues $[{}^{\boldsymbol{S}}\lambda_i^{alg}, {}^{\boldsymbol{S}}\lambda_i]$, gives raise to a cross of two orthogonal lines. The eigenvalues are also the radii of an ellipse aligned with the principal directions. If different colours for the combination of cross and ellipse are assigned for $\boldsymbol{S}^{alg}$ and $\boldsymbol{S}$, the linear sweep between the corresponding curves provides the complex glyph visualisation in Figure 9.

This visualisation tool indeed incorporates most of the advantages of the different techniques that have been discussed before. It allows, on the one hand, an excellent detection of regions in which large modifications occur. On the other hand, a detailed physical-based insight can be obtained by zooming-in, offering information both on magnitude and rotation. The motivation for nested visualisation can be verified by looking at Figure 10, which demonstrates that no single visualisation is usually capable of giving sufficient insight into all interesting aspects present in the data.

4 Conclusions & Outlook

In the first part of this paper, we have presented the essential ingredients for a thermodynamically consistent time-stepping scheme for finite elasto-plasto-dynamics, whereby the conservation properties are directly related to the approximation of related time-integrals. In this context, a modified quadrature rule has been applied based on a so-called elastic-enhanced algorithmic stress tensor. In the second part, special emphasis has been placed on the investigation of the spatial distribution of the resulting difference between the stresses of the continuum model and the enhanced stresses for the time-stepping. Thereby, it has been shown in previous work that an 'ad hoc' visualisation is not able to provide satisfying information. Therefore, we have devised visualisations of both abstract and physically based measures in the spatial context of the simulated domain. The results help revealing the intrinsic qualities of the data, especially by pointing out regions of interest. Indeed, the developed visualisation approaches provide a deeper insight into the numerical behaviour of the algorithmic stress tensor and, consequently, enable a better understanding of the discussed integration algorithms.

In future work, the discussed results, like influence of the time-step size or clustering of the corrections, should be verified for further data sets. Moreover, we plan to incorporate the time dimension, looking at the evolution of the corrections based on the here proposed visualisation techniques. Thereby, especially the question of time continuity of the difference between both tensor fields seems to be essential.

Acknowledgements Financial support by the German Research Foundation DFG within the International Research Training Group 1131 'Visualisation of Large and Unstructured Data Sets. Applications in Geospatial Planning, Modeling, and Engineering' is gratefully acknowledged by the authors.

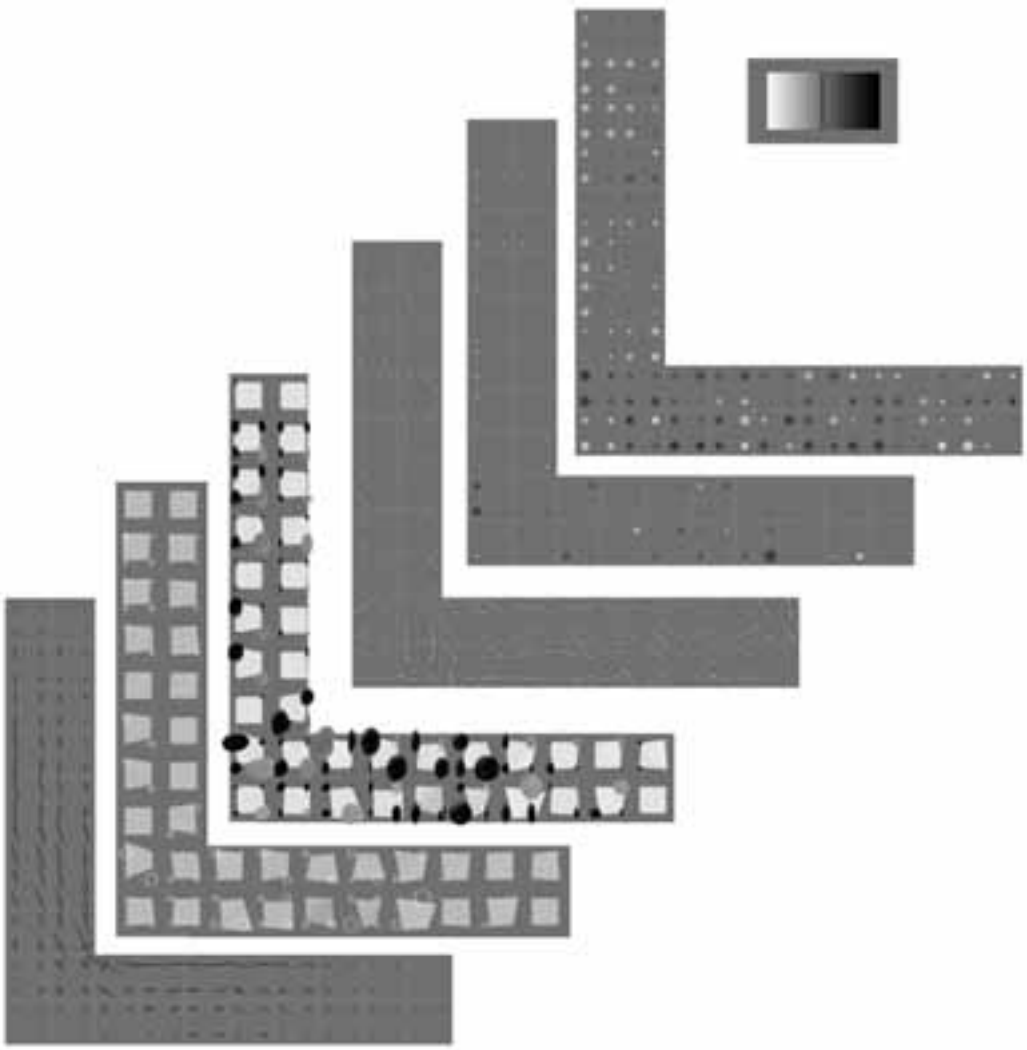

Figure 10: A collection of all presented visualisation tools applied to the same data set and time step (reproduced in colour on p. 190).

References

[Arm06] F. Armero. Energy-dissipative momentum-conserving time-stepping algorithms for finite strain multiplicative plasticity. *Computer Methods in Applied Mechanics and Engineering*, 195:4862–4889, 2006.

[BS01] P. Betsch, P. Steinmann. Conservation properties of a time FE method. Part II: Time-stepping schemes for nonlinear elastodynamics. *International Journal for Numerical Methods in Engineering*, 50:1931–1955, 2001.

[Gonz00] O. Gonzalez. Exact energy and momentum conserving algorithms for general models in nonlinear elasticity. *Computer Methods in Applied Mechanics and Engineering*, 190:1763–1783, 2000.

[GBS05] M. Gross, P. Betsch, and P. Steinmann. Conservation properties of a time FE method. Part IV: Higher order energy and momentum conserving schemes. *International Journal for Numerical Methods in Engineering*, 63:1849–1897, 2005.

[GGH*97] H. Guo, H. Gao, R. W. Hendricks, R. K. Batra, Y. Lavin, Y. Levy, and L. Hesselink. Visualization of Triaxial Residual Stress Tensors Near Welds in HSLA-100 Steel. *International Conference on Residual Stresses-5*, Linkoping, Sweden, June 1997.

[Jac99] R. Jacobson. *Information Design*. The MIT Press, 1999.

[ML02a] X. Meng, T. Laursen. Energy consistent algorithms for dynamic finite deformation plasticity. *Computer Methods in Applied Mechanics and Engineering*, 191:1639–1675, 2002.

[Kin04] G. Kindlmann. Visualization and Analysis of Diffusion Tensor Fields. *PhD thesis*, University of Utah, 2004.

[MMS06] R. Mohr, A. Menzel, and P. Steinmann. Galerkin-based time integrators for geometrically nonlinear elasto-plastodynamics – Challenges in modeling and visualization. In *Visualization of Large and Unstructured Data Sets, GI-Edition Lecture Notes in Informatics (LNI)*, S-4:185–194, 2006.

[MMS07a] R. Mohr, A. Menzel, and P. Steinmann. Conservation properties of Galerkin-based time integrators for geometrically nonlinear elasto-plasto-dynamics. In Proceedings of *IMPLAST – Symposium on Plasticity and Impact Mechanics*, Bochum, 2007.

[MMS07b] R. Mohr, A. Menzel, and P. Steinmann. Conservation properties of Galerkin-based time-stepping schemes for finite elasto-plasto-dynamics. In Proceedings of *COMPLAS IX – International Conference on Computational Plasticity*, Barcelona, 2007.

[MMS07c] R. Mohr, A. Menzel, and P. Steinmann. A consistent time-FE method for large strain elasto-plasto-dynamics. Submitted for publication, 2007.

[New59] N. Newmark. A method of computation for structural dynamics. *ASCE Journal of the Engineering Mechanics Division*, 85:67–94, 1959.

[NJP05] A. Neeman, B. Jeremic, and A. Pang. Visualizing Tensor Fields in Geomechanics. *IEEE Visualization*, 2005.

[NSP06] L. Noels, L. Stainier, and J. Ponthot. An energy momentum conserving algorithm using the variational formulation of visco-plastic updates. *International Journal for Numerical Methods in Engineering*, 65:904–942, 2006.

[ST92] J. Simo, N. Tarnow. The discrete energy-momentum method. Conserving algorithms for nonlinear elastodynamics. *Zeitschrift fuer Angewandte Mathematik und Physik (ZAMP)*, 43:757–792, 1992.

[WMN*02] C.-F. Westin, S. E. Maier, H. Mamata, A. Nabavi, F. A. Jolesz, and R. Kikinis. Processing and visualization of diffusion tensor MRI. *Medical Image Analysis*, 6(2):93–108, 2002.